Blocked drainpipes and smoking chimneys–discovery of new near-inertial wave phenomena in anticyclones

Leif N. Thomas[a] , James N. Moum[b] , Lixin Qu[c] , James P. Hilditch[a] ,
Eric Kunze[d] , Luc Rainville[e] , Craig M. Lee[e]

[a] *Department of Earth System Science, Stanford University, Stanford, CA, USA*
[b] *College of Earth, Ocean and Atmospheric Sciences, Oregon State University, Corvallis, OR, USA*
[c] *School of Oceanography, Shanghai Jiao Tong University, Shanghai, China*
[d] *NorthWest Research Associates, Seattle, WA, USA*
[e] *Applied Physics Laboratory, University of Washington, Seattle, WA, USA*

Corresponding author: Leif Thomas, leift@stanford.edu

ABSTRACT: Time-varying winds blowing over an eddying ocean generate near-inertial waves (NIWs) that tend to be trapped in anticyclones. Such anticyclones have been termed inertial chimneys in the past but have recently been renamed inertial drainpipes given their propensity to funnel NIW energy *downwards* to the deep ocean. Here, we present evidence of a semi-blocked inertial drainpipe where downward-propagating NIWs trapped in an anticyclone are partially reflected off the permanent pycnocline, returned toward the surface, and dissipated at the top of the seasonal pycnocline in a submesoscale filament of anticyclonic vorticity. Observations were made on the northern rim of an anticyclone in the Iceland Basin and include a high-resolution survey of velocity, hydrography, and microstructure. Upward-propagating NIWs were observed in a salty, submesoscale filament of anticyclonic vorticity near the edge of the eddy, potentially trapped there. Above the filament and at the top of the seasonal pycnocline, turbulence was enhanced over what could be attributed to local winds and surface cooling. Ray tracing suggests the filament could have channeled and focused trapped *upward*-propagating NIW, acting as an inertial chimney in a truer sense of the term, possibly intensifying the wave energy to a sufficient degree to sustain the observed turbulence. Numerical simulations of NIWs in anticyclonic vorticity and stratification representative of the observations suggest that the upward-propagating NIWs could have been generated by a wind event twelve days prior and reflected off a sharp jump in stratification at the base of the anticyclone. Here, the transition between the weakly-stratified winter mixed layer and permanent pycnocline partially reflects downward-propagating NIWs, limiting the inertial drainpipe effect.

1. Introduction

Some of the most energetic motions in the upper ocean are mesoscale eddies and wind-driven internal waves (e.g. Ferrari and Wunsch (2010) and references therein). The latter tend to have frequencies close to the inertial frequency, $f = 2\Omega \sin\lambda$ (where Ω is the Earth's angular velocity and λ latitude), and are known as near-inertial waves (NIWs). The dynamics of NIWs are controlled by Earth's rotation through the Coriolis force, but variations in the net spin of fluid caused by vertical vorticity, ζ, of a current, for example associated with the swirl of a mesoscale eddy, can greatly modify properties of NIWs. This effect is quantified by the effective inertial frequency $f_{eff} \approx f + \zeta/2$ which is lower in anticyclones and higher in cyclones (Kunze 1985). As such, NIWs can oscillate at lower frequencies within an anticyclone and thus lag NIWs outside of the eddy where f_{eff} is higher. This detuning implies that wind-driven NIWs are focused into anticyclones and downward out of the mixed layer into the pycnocline. Observational evidence of this phenomenon has been documented starting in the 1980s (e.g., Kunze and Sanford 1984; Kunze 1986) up to the present day (see Essink et al. (2022) for a particularly compelling example in a Kuroshio anticyclonic eddy). The phenomenon was coined the *inertial chimney* effect by Lee and Niiler (1998) but has recently been renamed the *inertial drainpipe* effect by Asselin and Young (2020) to more accurately evoke the image of downward energy propagation in anticyclones.

The preferential flux of NIW energy into anticyclones implies that there must be energy loss mechanisms within the eddies to maintain equilibrium. Several possible energy sinks are schematized in Fig. 1. As surface-forced NIWs propagate downward in weakening anticyclonic vorticity, they encounter a critical layer where their vertical wavelength and group velocity shrinks so that they stall and amplify (Kunze 1985, 1986). Microstructure observations supporting loss of NIW energy to a turbulent dissaptive sink in critical layers have been reported at the base of Gulf Stream warm-core rings (Lueck and Osborn 1986; Kunze et al. 1995) and towards the bottom of anticyclones in the Mediterranean, Arctic, and Norwegian Seas (Cuypers et al. 2012; Kawaguchi et al. 2016; Fer et al. 2018). The mechanism could be widespread and might contribute to seasonal variations in mixing in the thermocline (Whalen et al. 2018).

Apart from losing energy to turbulence, NIWs in critical layers can transfer energy to the anticyclone via wave-mean flow interactions (Fig. 1(i)) or to higher-frequency internal waves through wave-wave interactions (Kunze et al. 1995). These higher-frequency waves are not necessarily bound to the anticyclone and could radiate energy away from the eddy (Fig. 1(ii)).

In this article, we describe a fourth sink for NIWs in an inertial drainpipe. It involves the partial reflection of the downward-propagating NIWs off the jump in stratification that can be found near the base of anticyclones and subsequent dissipation of the resulting upward-propagating NIWs near the surface (Fig. 1(iv)). Evidence for this energy pathway comes from observations of NIWs and turbulence on the edge of an anticyclone in the Iceland Basin, which are described below and interpreted using theory and idealized numerical simulations.

2. Overview of observations

The measurements were made in the Iceland Basin as part of the Near-Inertial Shear and Kinetic Energy in the North Atlantic experiment (NISKINe), the goal of which was to study NIWs in the Iceland Basin from wind generation to turbulent dissipation, including their interactions with the mesoscale and submesoscale eddy field. The observations presented here are from a survey termed the ”Fence Survey” conducted June 9-12, 2019 from the *R/V Neil Armstrong*. The survey followed an array of drifting assets including EM-APEX floats (e.g. Girton et al. 2024) that were deployed towards the outer edge of an anticyclone. The focus of this article will be on observations made from the ship as it transected the eddy’s rim while traveling downstream with the array of drifting assets. These include measurements of velocity from 150-kHz and 300-kHz ship-mounted ADCPs in the upper 400 m and 100 m, with bin size of 8 m and 2 m, respectively, processed using UHDAS (https://currents.soest.hawaii.edu/). Hydrography was collected using a Triaxus-towed, undulating profiler. Triaxus profiled from the sea surface to 170 m depth at vertical speeds of 0.8-1.0 m s^{-1} and tow speeds of 2-4 m s^{-1}. The profiler carried an extensive payload of physical and bio-optical sensors, including a Seabird SBE 9 plus CTD equipped with dual, pumped temperature (SBE 3plus) and conductivity (SBE 4C) sensors sampled at 24 Hz. Hydrography from the Triaxus CTD was augmented by six full-depth casts with the ship’s SeaBird TSG CTD along a line that transected the anticyclone June 8-9, 2019 (Fig. 2(a)). A GusT probe (Becherer et al. 2020) attached to Triaxus was used to measure temperature microstructure of flow undisturbed by the instrument package and from which turbulence diffusivity (K_T) and the dissipation rate of turbulence kinetic energy (ϵ) were estimated. The GusT probe is a miniaturized version of a χpod

(Moum and Nash 2009) which has now seen extensive use on oceanographic moorings (Moum et al. 2023). Implementations of χpods to date have been on fixed platforms where the fluid moves past the sensor. In this implementation, the sensor moves through the fluid. Spectral fits in the inertial-convective subrange (Zhang and Moum 2010) were used to infer estimates of K_T and ϵ.

3. Anticyclone and wind forcing

The background flow in the study region is characterized by an anticyclone with maximum velocities ~ 0.5 m s^{-1} and radius ~ 75 km. The core of the anticyclone is filled with remnant winter water and weak stratification. More specifically, the square of the buoyancy frequency, $N^2 = -g/\rho_o \partial\sigma_t/\partial z$ (where g is the acceleration due to gravity, ρ_o a reference density equal to 1000 kg m^{-3}, σ_t the potential density, and z is the vertical coordinate), in these waters can be less than 1×10^{-6} s^{-2} (Fig. 2(a)). The winter water is bounded above and below by more stratified waters. At the base of the winter water layer is an abrupt 40-fold increase in N^2 crossing into the permanent pycnocline. The winter water layer is also capped by a seasonal pycnocline between 10-60 m. In the seasonal pycnocline N^2 can exceed 1×10^{-4} s^{-2} (Fig. 2(a)). A $\sim$ 10 m thick mixed layer tops all three of these layers.

The permanent pycnocline has a bowl-like shape in the anticyclone, rising from a depth of 700 m in the eddy center to 400 m at its edge (Fig. 2(a)). The corresponding tilt in the pycnocline results in a surface-intensified anticyclonic circulation. However, vertical gradients in the circulation are mostly confined to the depths of the permanent pycnocline (i.e., between 500 and 1000 m) such that, within the winter water layer, the anticyclonic circulation is fairly barotropic on the larger scale of the eddy.

The Fence Survey revealed that the anticyclone also has finer-scale filamentary features near its rim. Here, filaments less than 5-km wide and $\sim$ 40-km long were evident in both salinity and vertical vorticity (Fig.3). Vertical vorticity was approximated as $\zeta = \partial v_{al}/\partial x_{cs}$, where v_{al} is the along-stream component of the flow on each section and x_{cs} is a cross-stream coordinate defined to be perpendicular to the maximum depth-averaged flow on the section and increases towards the center of the eddy. Vertical vorticity co-varies with the salinity, with cyclonic vorticity tending to coincide with fresher waters, while the filaments of saltier water are correlated with stronger anticyclonic vorticity (Fig. 3). Saline filaments do not reach the surface but are capped by the seasonal pycnocline. Anticyclonic vorticity in the filaments is also weaker near the surface (Fig. 3(d)) which has important implications for the propagation of NIWs, as will be discussed in section 4.

Winds during the field campaign were conducive for generating NIWs. The strongest wind event occurred during the passage of storm on May 30, yielding a wind-stress that approached 1 N m^{-2} (Fig. 2(b)). After the storm, before and during the Fence Survey (starting on June 9), the winds were weaker and steadier, so less prone to creating NIWs. To quantify how effective the winds were at generating NIWs, an estimate for the amount of kinetic energy injected into near-inertial motions was calculated using a slab mixed-layer model forced by the observed winds and assuming a mixed-layer depth of 10 m, a value representative of what was observed during the cruise (Pollard and Millard 1970). The model integrates the linear momentum equations averaged over the mixed layer and uses Rayleigh damping with a damping coefficient of $0.1f$. Velocity from the model and wind-stress were used to estimate the time-integrated wind-work, a measure of the kinetic energy input to near-inertial motions by winds. The model indicates that the largest and most abrupt injection of kinetic energy by the winds occurs during the 30 May wind-event (Fig. 2(c)), suggesting that the storm was an effective NIW generator. Surveys on the southwest edge of the anticyclone (near 57° 48' N, 23° 30' W) made within a few days of the storm revealed acceleration of near-inertial motions in the mixed layer and seasonal pycnocline, as well as their subsequent decay through downward radiation of NIWs into the anticyclone (Thomas et al. (2020, 2023) and Thomas et al in this special volume).

4. Evidence of upward-propagating NIWs and a true inertial chimney

Banded patterns in vertical shear, a signature of NIWs, were observed on several of the sections of the Fence Survey. The shear bands were angled down towards the center of the anticyclone (Fig. 4(b)). The section was completed in a fraction of an inertial period, T_i = 14 hours, (i.e. $0.18T_i$ or 2.5 hours). Therefore, the shear can be interpreted as a snapshot of a NIW beam. The tilt in the shear bands indicates possible directions of wave energy propagation, either down and towards the center of the eddy, or up and towards the edge of the eddy. The ambiguity in the direction of energy propagation can be resolved by examining the rotary behavior of the vertical shear vector (u_z, v_z) with depth, $\phi_{shear} = \tan^{-1}(v_z, u_z)$ (Leaman and Sanford 1975). In the northern hemisphere, clockwise rotation with depth is a signature of downward energy propagation as expected for wind-generated NIWs (D'Asaro and Perkins 1984). But below 100 m depth for $x_{cs} = -10$ km, where the shear bands are most prominent, the shear vector rotates counterclockwise with depth, implying that wave energy is propagating upward toward the surface (Fig. 4(a)). This finding raises several questions. In particular, where did the upward-propagating waves originate, how were they generated, and what might they do as they approach the sea surface? We reserve the first two questions for section 6 and address the last question here using ray tracing.

Ray tracing is a technique used to estimate the path waves travel in an inhomogenous medium (Lighthill 1978). It involves using the dispersion relation for the particular wave of interest to calculate the group velocity and its variations in space. The group velocity can be integrated in time to trace the path of the wave, known as a ray. For NIWs in a background flow, the dispersion relation depends on stratification, the effective inertial frequency, f_{eff}, and other factors related to the vertical shear of the background flow, which are of secondary importance for this particular anticyclone (Mooers 1975; Kunze 1985; Whitt and Thomas 2013). If the waves have any along-stream propagation, they can experience Doppler shifting which can distort ray paths (Olbers 1981). To simplify the analysis, we assume that the waves only propagate in the across-stream and vertical directions and neglect Doppler shifting.

On the section of interest described above, there are large variations in stratification and more subtle, although significant, modulations in f_{eff} which can affect the propagation of NIWs. The effective inertial frequency, like vorticity, co-varies with the salinity. In particular, regions where $f_{eff} < f$ tend to coincide with the saltier filaments (for example near x_{cs} -10, 0, 10 km in Figs. 3(c) and 4(c)). We focus the ray-tracing calculation on the saltier filament centered around $x_{cs} = -10$ km since this is where the NIW beam is observed. According to the dispersion relation for NIWs, internal waves with a subinertial frequency of $0.97f$ are permitted in this region where $f_{eff} < 0.97f$. The rays of these subinertial waves are trapped in the filament and reflect off their separatrix, i.e. the $f_{eff} = 0.97f$ surface (Fig. 4(b)-(c)). This suggests that these saltier filaments with anticyclonic vorticity funneled upgoing NIW energy. In this sense, we might consider these regions to act as inertial chimneys. The rays that propagate upwards and outwards (i.e. towards decreasing x_{cs}) run nearly parallel to the shear bands, implying that the observed NIWs have an intrinsic frequency close to $0.97f$. These waves would be evanescent in regions where $f_{eff} > 0.97f$

such as the fresher filament with more positive vorticity near $x_{cs} = -5$ km. The weakening of the vertical shear there supports this notion (Figs. 3(c) and 4(b)-(c)).

Anticyclonic vorticity anomalies in the saltier filaments weaken within the seasonal pycnocline. This vertical structure of the vorticity has potentially important consequences for the amplitude of upward-propagating, subinertial NIWs. The increase in ζ towards the surface bends the separatrix for these waves into a concave-down shape. This geometry, combined with increasing stratification in the seasonal pycnocline, focuses rays. Such lateral focusing reflections amplify internal waves. In addition, amplification could also arise from a vertical critical layer at the top of the filament if the NIWs cannot escape its confines. Having said this, these interpretations should only be considered suggestive since the assumptions used in the ray-tracing calculation may not hold for this flow (i.e. the lateral wavelengths of the NIWs appear to be larger than the filament widths and Doppler shifting may not be negligible). However, if there is NIW focusing in the filaments, and if the amplification is sufficiently large, it could trigger wave breaking and turbulence. There is evidence for this in the observations.

5. Enhanced mixing atop the chimney

Microstructure measurements from the GusT probe mounted on Triaxus suggest that the upward-propagating NIWs observed in the section generate turbulence. Sections of potential density (Fig. 5b) and squared current shear (Fig. 5c) are overlain by colored dots indicating the magnitude of ϵ along the Triaxus trajectory. These indirect estimates of ϵ based on fast thermistor measurements cannot be made in the absence of stratification. Hence, mixed-layer values, for example, are flagged so that they are not plotted or included in averages. For reference, the red line in Fig. 5e represents an estimate of what we might expect for tendencies of ϵ in the mixed layer, based on law-of-the-wall scaling using the measured wind-stress to determine the friction velocity u_*. The latter is an underestimate near the surface as it does not account for the effects of surface wave breaking and other surface processes and perhaps an overestimate at greater depths where stratification acts to suppress the law of the wall.

At the base of the mixed layer and above the concave-down separatrix (indicated by the $f_{eff} = 0.97f$ contour in Fig. 4(b)-(c)) over x_{cs} = [-15 -5] km (the top of the chimney), lies a region of enhanced ϵ and K_t relative to background values (Fig. 5f). Here, average dissipation rates approach 10^{-6} m^2 s^{-3}, which is nearly 10 times larger than ϵ averaged across the surrounding waters. Shear and stratification are stronger above the chimney as well. At the mixed-layer base, average N^2 is greater by a factor of about 2 while average $Sh^2 = u_z^2 + v_z^2$ is greater by more than a factor of 4, bringing the average Richardson number, Ri, nearer to 1/4, or tending reduced shear $Sh^2 - 4N^2$ to values > 0, suggesting significant potential for shear instability (Fig. 5d). The true vertical resolution of horizontal velocity shear estimated from the 300-kHz ADCP is coarser than its 2-m bins, therefore Sh^2 is likely underestimated so that actual values of Ri may be smaller and reduced shear greater than suggested by Fig. 5d.

While small peaks in turbulence have been observed at the base of ocean mixed layers (Lombardo and Gregg 1989; Anis and Moum 1994), here observed values of ϵ approaching 10^{-6} m^{2}s^{-3} and $K_T > 0.03$ m^{2}s^{-1} are greater than previously reported, at least in open ocean conditions away from the equator. We also note that the surface buoyancy flux during this period associated with surface cooling is smaller than the averaged value of ϵ at the mixed-layer base by a factor of 10. A turbulent diffusivity of 1×10^{-2} m^2 s^{-1} would mix a layer 10 m thick in 2.5 hours. The fresher waters in the mixed layer observed above the streamer of fresh water in the pycnocline in the high dissipation region (e.g. Fig. 3(c), $x_{cs} < -10$ km) could be a consequence of such mixing.

It seems plausible that the enhanced turbulence at the mixed-layer base atop the chimney (Fig. 4) derives its energy from the upward propagating NIWs. If so, in a steady state, dissipation would be balanced by convergence of the wave energy flux, F_e (similar to what Kunze et al. (1995) found for downward-propagating NIWs approaching a critical layer at the base of a Gulf Stream warm-core ring). With this balance in mind, integrating the dissipation profile in the vertical can yield an upper bound on the wave energy flux needed to sustain the dissipation, i.e. $F_e = \int_z^0 \rho_o \epsilon dz$. Estimates of ϵ in the mixed layer are set to zero in this integral, since ϵ is not well constrained in the mixed layer and the objective of this calculation is to quantify the jump in wave energy flux in the seasonal pycnocline that would drive the inferred enhanced dissipation there. The integration implies that an upward wave energy flux of order 10 mW m^{-2} would have to be absorbed in the seasonal pycnocline to support the observed dissipation if no other sources of energy were available for the turbulence. The plausibility of a NIW energy flux of this magnitude given the properties of the NIW field in the Iceland Basin is discussed in section 7.

6. Possible sources of the upward-propagating NIWs

We now attempt to constrain the origin of the upward-propagating NIWs observed on the section. Three hypotheses are explored: one, upward radiation of semi-diurnal internal tides (which are near-inertial at these latitudes), two, reflection of wind-driven NIWs off the bottom, and three, reflection of wind-driven NIWs off jumps in stratification.

a. Semi-diurnal internal tides

Semi-diurnal internal tides have been observed to emanate from the nearby Reykjanes Ridge (Vic et al. 2021). At the latitude of the survey, semi-diurnal tides have a frequency of $1.13f$ which, although close to f, would generate NIWs with shear bands of slope $\sqrt{\omega_i^2 - f_{eff}^2}/N$ roughly twice as large as the observed slope for an intrinsic frequency $\omega_i = 1.13f$. However, it is possible that the intrinsic frequency of the semi-diurnal tides could be modified by the mean current of the anticyclone through a Doppler shift. In particular, if ω_i were shifted below f, then the shear bands could be attributed to semi-diurnal tides. For this to happen, the internal tide would need to propagate with the mean current and have a wavelength of a few hundred kilometers in the along-stream direction. It is possible that these conditions were met in the anticyclone. For example, if the semi-diurnal tides were radiated directly from the Reykjanes Ridge, they would most likely propagate with the eastward mean current on the northern edge of the anticyclone since the ridge is to the west of the eddy. Thus we cannot rule out the semi-diurnal internal tides as a source of energy for the observed upward-propagating NIWs.

b. Reflected wind-driven near-inertial waves

Alternatively, if the NIWs were driven by winds at the surface, the upward-propagating waves that we observed must have reflected off either an interior fluid boundary or the sea floor. We use wave travel time to determine which scenario is more plausible under the assumption that the NIWs on the section were generated by the strong wind-event on May 30, 2019 when a large amount of near-inertial energy was injected into the ocean (Fig. 2(c)) after which downward-radiating NIWs were observed (Thomas et al. 2020, 2023) and not an earlier storm. This wind-event occurred ~ 12 days prior to the measurements of the upward-propagating NIWs. Therefore, reflection scenarios with wave travel times that significantly exceed 12 days are ruled out.

Travel times were estimated using ray tracing. For this calculation, hydrography from the deep CTD cast closest to the center of the anticyclone was used for the stratification (Fig. 6(c)). A downgoing ray was initiated at a depth of 150 m with a vertical wavelength of 400 m and subinertial frequency $0.97f$. We assume that vorticity of the background flow is uniform with a value of $-0.1f$ and the stratification is laterally-homogeneous. With these wave parameters and background flow, ray tracing predicts that by 12 days a NIW packet only reaches a depth of 700 m, which is well short of the bottom at $\sim$ 3000 m (Fig. 6(a)), let alone a return to the surface. A wave with vertical wavelength shorter than 400 m, more similar to what was observed by Thomas et al. (2020) shortly after the 30 May wind event, would travel even more slowly. Thus, we can eliminate bottom reflection as the source of the observed upward-propagating NIWs, if the waves were forced by the May 30th wind event. If the waves were forced by an earlier storm, however, bottom reflection of NIWs cannot be discounted.

Ray tracing also predicts that the vertical wavelength of the NIW increases from its initial value of 400 m as the NIW transits the weakly-stratified core water, then sharply decreases from $\sim$ 1500 m to less than 500 m when the wave crosses the jump in stratification near 600 m (Fig. 6(b)). This change in wavelength occurs over a distance much smaller than the wavelength itself, which is in clear violation of the WKBJ approximation that forms the basis of ray tracing. Therefore, in the proximity of jumps in stratification of this magnitude, ray tracing should not be used to infer properties of the wave field, but instead full solutions to the wave equation should be sought. Such solutions have been calculated for similar stratification profiles and predict that a fraction of the downward-propagating wave energy is reflected off jumps in stratification (see Appendix-Box-).

1) Reflection off stratification jump–idealized simulations

To further illustrate the plausibility of reflection of wind-driven NIWs off the stratification jump at the top of the permanent pycnocline at 600 m as the source of the upward-propagating NIWs, we ran idealized simulations to illustrate the mechanism using the Regional Ocean Modeling System (ROMS) (Shchepetkin and McWilliams 2005). The model domain is 240 $km \times 9$ km with a uniform depth of 2400 m. Horizontal resolution is 500 $m \times 500$ m, and there are 256 depth layers. The depth grid is surface-refined so that the spin-up of near-inertial motions near the surface can be captured. The Coriolis frequency is constant and set to f at 58° N. The background velocity is a double jet mimicking the azimuthal flow of the observed anticyclonic eddy (see Fig. 7a). The domain is set to be extremely narrow in the along-jet direction with few grid points under the assumption that variation in the along-jet direction is small. The vertical vorticity in this two-dimensional "anticyclone" is $-0.05f$. The observed wind-stress from 29 May to 1 June (e.g. Fig. 2b) is used to force the model for the first four days, and then wind forcing is set to zero for the remaining six days of the simulation. The background density has two different configurations for comparison. One uses the observed stratification from the deep CTD cast (Fig. 6), while the other uses a modified stratification profile without the stratification jump at 600 m (see Fig. 7b).

Within the anticyclone (i.e., between 90 and 160 km), vertical shear takes a banded structure, with the shear bands tilting down and towards the center of the anticyclone, a feature characteristic of NIWs trapped in an inertial drainpipe (Fig. 7(c)-(f)). There are also downgoing NIWs outside of the anticyclone. These are associated with NIWs that radiate away from the regions of cyclonic vorticity on the outer edges of the jet. The difference in shear between the simulation with and without the stratification jump quantifies adjustments to the NIW field due to the abrupt change in N^2. Above the permanent pycnocline ($z > -600$ m), a pattern consistent with upward-propagating NIWs is visible, with shear bands that tilt up and towards the center of the anticyclone (e.g Fig. 7(g)-(h))[1] Three days into the simulation (corresponding to two days after the wind event on 30 May), a NIW that had reflected off the stratification jump has returned to the surface (e.g Fig. 7(g)). This NIW has a long vertical wavelength ($\sim$ 1200 m) and propagates rapidly. A NIW with a 200-m vertical wavelength similar to the observations (e.g. Fig. 4(b)) would propagate at one sixth the speed of this NIW (if the frequencies of the waves were the same), implying that a NIW with a 200-m vertical wavelength would reach the surface $\sim$ 12 days from the wind event after reflecting off the jump in stratification, a time scale consistent with the observations.

The locations where the upgoing NIWs in the anticyclone reach the surface ($\sim$ 120 km and $\sim$ 140 km) are towards the center of the eddy, unlike the observed upgoing NIWs which were found near the edge of the eddy. These locations are set by the particular paths along which NIWs propagate. These ray paths are sensitive to many factors, such as the detailed spatial structure of vorticity and stratification in the eddy and its filaments, the horizontal direction waves propagate (which might not be perfectly radial), factors that are not expected to be captured in these idealized simulations.

[1]To better visualize the propagation of the NIWs in the simulations, an animation of panels (c)-(h) of Fig. 7 can be found in the supplementary material.

The objective of these simulations is not to determine the locations where the upgoing NIWs reach the surface, but to demonstrate how NIWs can reflect from a jump in stratification representative of the observations.

7. Discussion

Assuming that the observed upward-propagating NIWs are wind-driven NIWs reflecting off the seasonal pycnocline, the question still remains if such waves are sufficiently energetic to explain the high dissipation rates at the base of the mixed layer observed within the NIW beam. If balanced by an influx of wave energy into the seasonal pycnocline, it was previously shown that the inferred dissipation would require a wave energy flux of order 10 mW m^{-2}. Downward NIW energy fluxes shortly after the wind-event on May 30, 2019 are an order of magnitude weaker than this (Thomas et al. 2023). In addition, NIWs are only partially reflected off a stratification jump of the strength seen at 600 m. As discussed above, the upward energy flux of the reflected waves should be around half the energy flux of the downgoing NIW and would correspond to a fraction of a mW m^{-2}. However, these waves could still power the observed dissipation if wave focusing in filaments locally intensifies the NIWs to a sufficient degree. For this to happen, the cross-sectional area of beams of upward-propagating NIWs would have to shrink by more than a factor of ten as they transit from the permanent pycnocline to the top of the $\sim$ 5-km wide vorticity filaments. The two-dimensional, idealized simulations suggest that beams of upward-propagating NIWs span $\sim$ 50 km near 600 m (Fig. 7(h)), approaching the ten-fold larger widths needed to support the requisite intensification in energy flux near the surface.

The observations, theory, and simulations described here paint a different picture of NIW behavior in anticyclones than the conceptual models of inertial drainpipes and critical layers at the base of the anticyclones. Namely, the energy sink for NIWs in anticyclones can shift to the upper ocean when downward-propagating NIWs reflect off the permanent pycnocline and are focused, amplified and dissipated in filaments of anticyclonic vorticity. The reflection partially blocks an inertial drainpipe, and the submesoscale, anticyclonic filaments that focus the upward-propagating NIWs act like a surface-layer waveguide which could be described as an inertial chimney.

Clearly, this NIW behavior is shaped by the particular characteristics of the anticyclone we observed, specifically, an abrupt transition in stratification between a well-mixed remnant winter water layer and the permanent pycnocline that is located higher in the water column than the critical layer, and submesoscale filaments of vorticity that weaken in magnitude towards the surface. Having said this, anticyclones are often characterized by core waters with anomalously weak stratification bounded below by a stratified layer (for example, Gulf Stream warm-core rings and mode-water eddies) and filamentation of vorticity on the edge of eddies is common. Thus, the confluence of conditions that we observed may not be too unusual. In the Japan/East Sea for example, there have been observations of upward-propagating NIWs in anticyclones with a similar stratification profile to that described here (Byun et al. 2010).

In the Iceland and Irminger Basins, velocity profiles made with floats over two consecutive years spread throughout the region show a widespread dominance of upgoing NIWs in June through August (Kunze et al. 2023). These floats sampled many different mesoscale environments, not just anticyclones, so the NIWs observed by the floats likely experienced a variety of propagation pathways different from the ones discussed in this article. The near-inertial signals measured by the floats could have been associated with semi-diurnal internal tides radiated from topographic ridges, a scenario that might also explain the upward-propagating NIWs that we observed (if they were Doppler shifted). It should be noted that the analyses of Kunze et al. (2023) were primarily focused on depths within the permanent pycnocline where reflections of downward-propagating NIWs off the top of the pycnocline are not obviously relevant. Nevertheless, the observations from the floats highlight how the weakly-stratified winter water layer and concomitant jump in stratification in the permanent pycnocline is a ubiquitous feature of the hydrography in the Iceland and Irminger Basins so may lead to reflections of downgoing NIWs across the basin.

Globally, it is estimated that the shear variance in downgoing internal waves exceeds the shear variance in upgoing waves by 30% in the upper 600 m of the ocean (Waterhouse et al. 2022). This implies that there is considerable energy in upward-propagating internal waves in the upper ocean. The source, fate, and regional variations of such waves is not well understood. The mechanisms that we have described here involving mesoscale eddies, internal reflections off jumps in stratification, and wave focusing in filaments of vorticity could contribute to shaping the submesoscale structure of the upgoing NIW and turbulence fields in the ocean. Quantifying their regional and global impacts would be of interest.

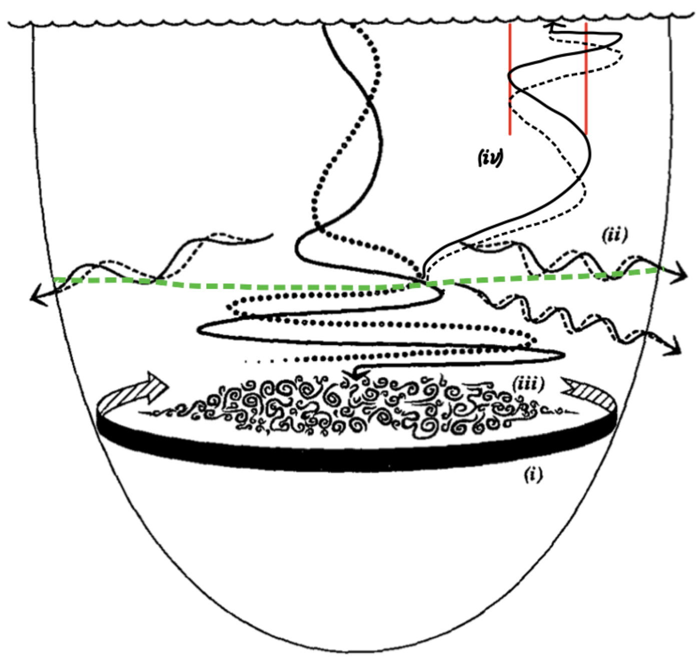

FIG. 1. Schematic illustrating four hypothesized sinks of NIW energy trapped in an anticyclone (adapted from Kunze et al. (1995)). A downward-propagating NIW focused in the center of an anticyclone via the inertial drainpipe effect has an east (solid line) and north (dotted line) velocity 90° out of phase such that the velocity vector spirals clockwise with depth. As the wave approaches the depth where its frequency is equal to $f_{eff} \approx f + \zeta/2$ (critical layer), its vertical wavelength and propagation speed shrink. Its energy increases until it is lost to either (i) the mean circulation, (ii) untrapped, higher-frequency internal waves, or (iii) turbulence. If the anticyclone has a jump in stratification (dashed green line), part of the NIW energy is reflected off the jump, partially blocking the inertial drainpipe (iv) with a velocity vector that spirals counterclockwise with depth. Submesoscale filaments with anticyclonic vorticity (red lines) on the edge of the eddy can focus the upward-propagating NIW in an inertial chimney, leading to wave amplification, breaking, and dissipation near the surface.

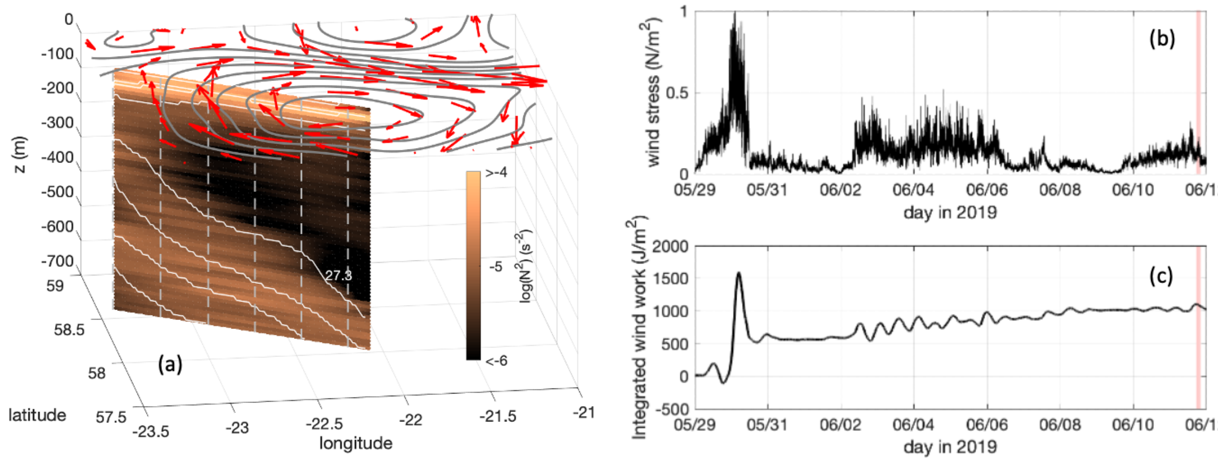

FIG. 2. Structure of the anticyclone that is the focus of this study and the wind-forcing during the field campaign. (a) The sea-surface height anomaly (from AVISO, grey contours), surface velocity (red vectors), potential density field (contoured in white every 0.1 kg m^{-3}), and N^2 (shading) in the anticyclone. The section of potential density was mapped using hydrography from six deep CTD casts taken at the locations indicated by the vertical dashed lines. Time series of (b) wind-stress observed from the ship during the cruise and (c) kinetic energy input to near-inertial motions by the winds estimated using a slab mixed-layer model. The vertical red lines in (b) and (c) indicate the time when the section with upward-propagating NIWs was collected (Fig. 4(b)).

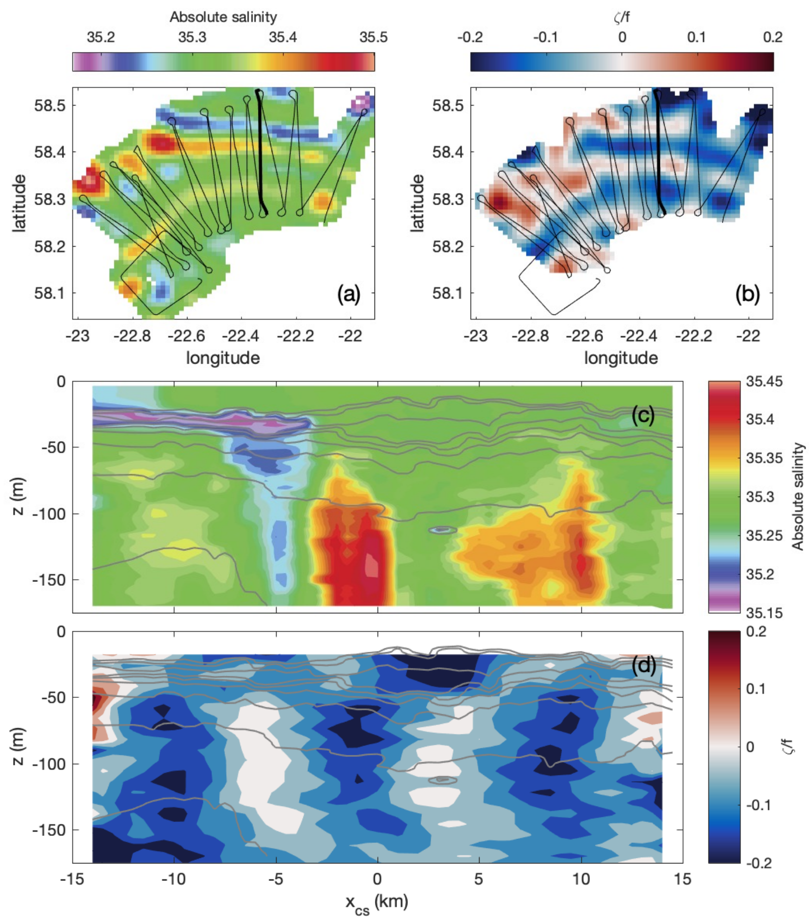

Fig. 3. Filamentary nature of salinity (a,c) and vorticity (b,d) fields observed on the Fence Survey along the northern rim of the anticyclone (ship track in black). Mapped plan-view sections at $z = -100$ m of (a) absolute salinity and (b) vertical vorticity normalized by f. Vertical sections of absolute salinity (c) and vertical vorticity normalized by f (d) along the transect indicated by the thick black lines in (a) and (b). Potential density is contoured in gray every 0.05 kg m^{-3} in (c)-(d). This is the same transect where the upward-propagating NIWs were observed (Fig. 4(b)). x_{cs} unconventionally increases towards the center of the eddy.

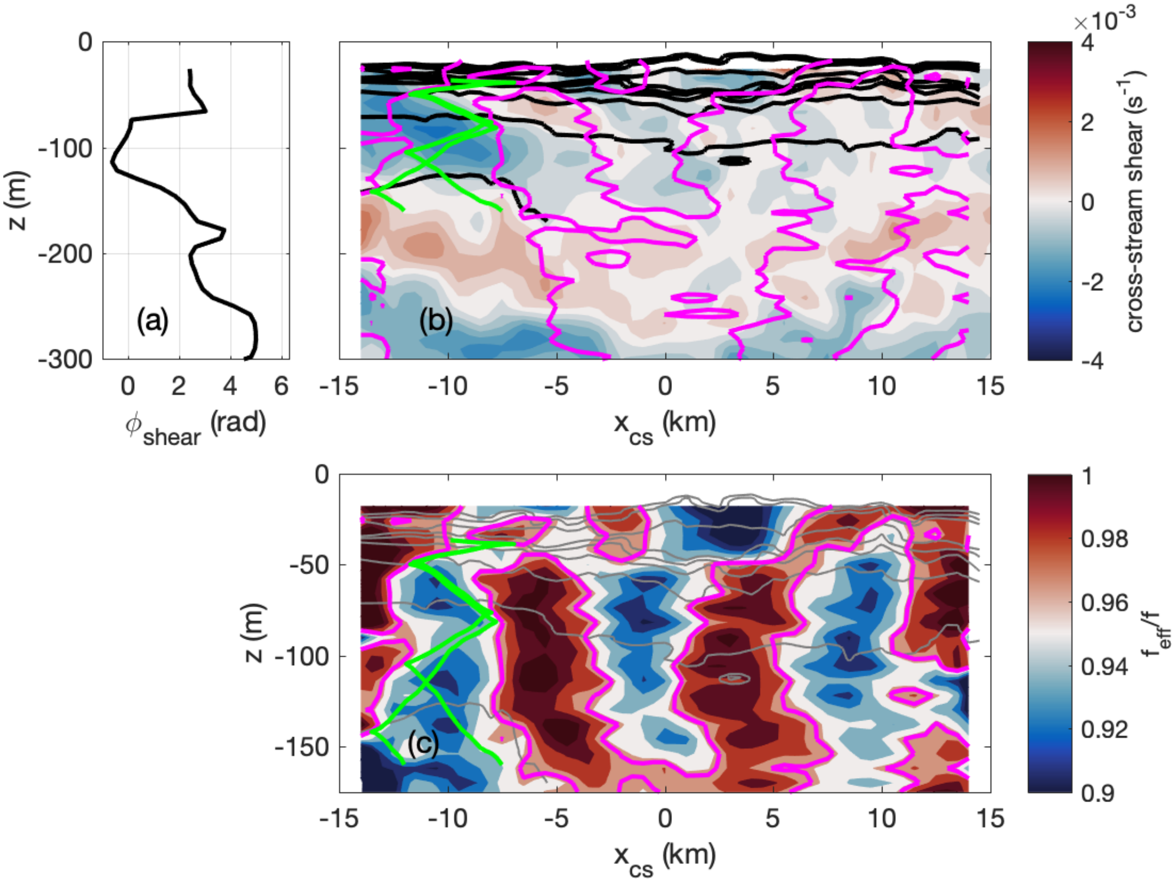

FIG. 4. Evidence for upward-propagating NIWs from the section indicated by the thick black line in Fig. 3(a)-(b) which was collected between 17:45-20:15 11 June 2019 UTC. (a) Angle that the vertical shear vector makes as a function of depth, $\phi_{shear} = \tan^{-1}(v_z/u_z)$ evaluated at $x_{cs} = -10$ km on the section shown in (b). A banded structure is seen in shear near $x_{cs} = -10$ km (colored in (b)). Beneath 100 m, the shear vector rotates counterclockwise with depth, consistent with upward-propagating NIWs. Two rays (green lines in (b) and (c)) tracing the path of upward-propagating NIWs with a frequency of $0.97f$ initiated at $z = -160$ m laterally reflect off locations where the effective inertial frequency is equal to the frequency of the wave, i.e. $f_{eff} = 0.97f$ (indicated by the magenta contours in (b) and (c)), and converge in the near-surface seasonal pycnocline (isopycnals are contoured in black every 0.05 kg m^{-3}). (c) The effective inertial frequency $f + \zeta/2$ normalized by f (color) and density (contoured at the same interval as in (b)) along the section.

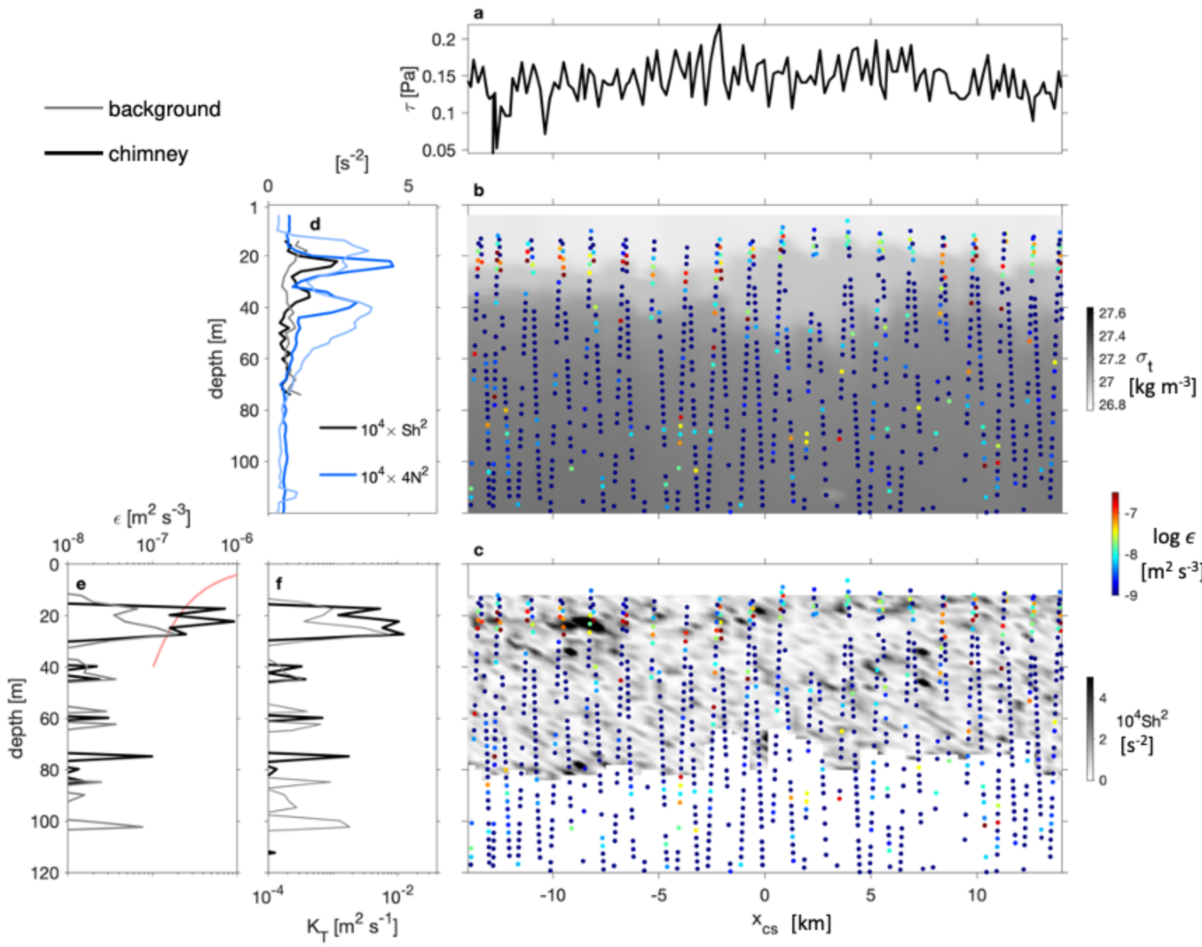

FIG. 5. Enhanced dissipation and mixing associated with the upward-propagating NIW in Fig. 4(b). (a) wind-stress, τ, time-series. (b) Depth-cross stream section of potential density, σ_t (grey scale). Colored dots in (b) and (c) represent 5 m depth-averaged estimates of ϵ from GusT probe on Triaxus. (c) Depth-cross stream section of squared current shear, $Sh^2 = u_z^2 + v_z^2$, from 300-kHz ship-mounted ADCP (grey scale). The ADCP is range-limited to 60 – 80 m in these waters. Colored dots representing ϵ in (b) are echoed in (c). Vertical profiles of (d) $10^4 \times Sh^2$ (black), $4N^2$ (blue), (e) ϵ, (f) K_T. In (d-f), thick lines represent spatial averages over [-15 -5] km representing the region of the inertial chimney (Fig. 4); thin lines represent the background average over [-5 15] km. In (e), the red line indicates a law-of-the-wall scaling for ϵ in the mixed layer where thermistor estimates of ϵ are not reliable.

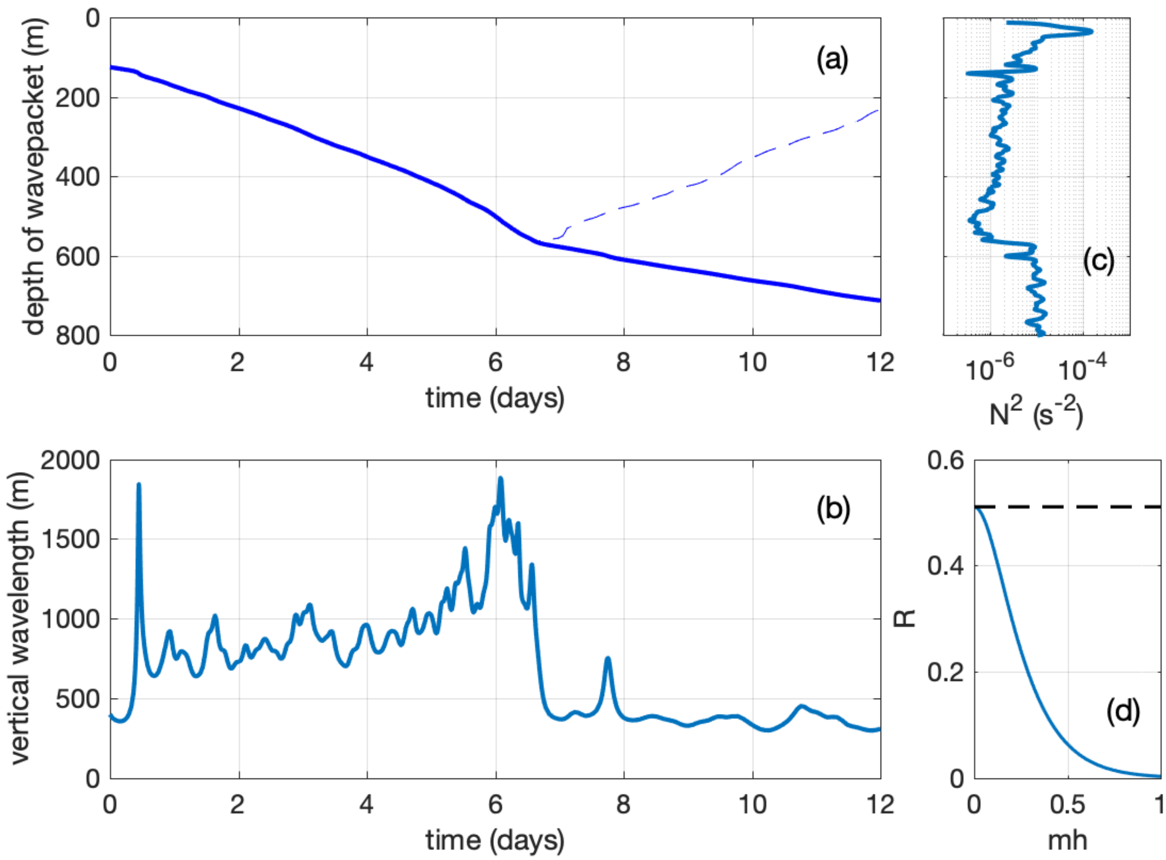

Fig. 6. Ray-tracing estimates of travel time and vertical wavelength of a NIW with frequency $0.97f$ propagating in an anticyclone with vorticity $-0.1f$ and stratification representative of the observations. Depth (a) and vertical wavelength (b) of an incident and transmitted (solid blue), and reflected (dashed blue) NIW wavepacket as a function of travel time. (c) Stratification profile within the anticyclone at 58° 5' N, 22° 10' W that was used in the ray-tracing calculation, with an abrupt jump at a depth near 600 m affecting wave properties. (d) Fraction of the wave energy flux reflected by a smooth six-fold increase in buoyancy frequency as a function of mh where m is the incident wavenumber and the buoyancy frequency increases with a $\tanh(z/h)$ transition region. The grey dashed line indicates the fraction reflected by a discontinuous six-fold jump (equation -Box-2).

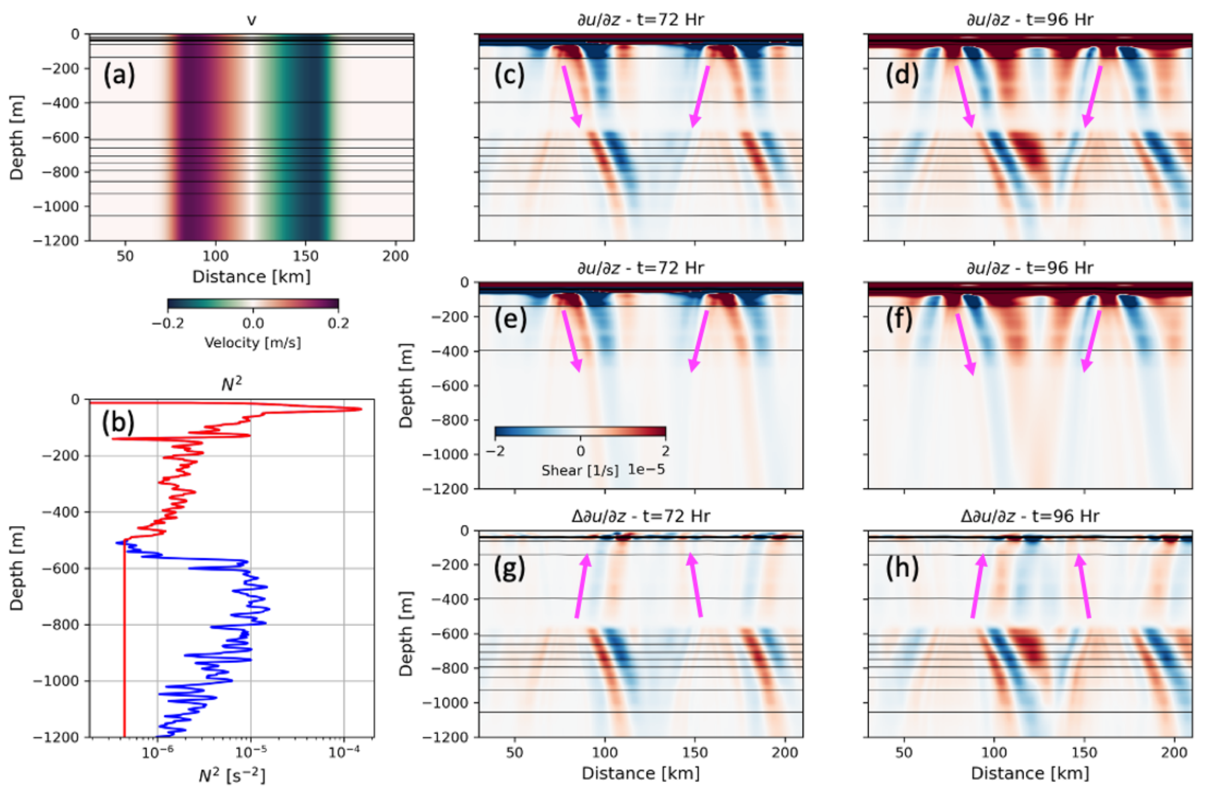

Fig. 7. Simulations illustrating how NIW generated by winds trapped in an anticyclone can reflect off a jump in stratification. (a) Structure of the velocity of the anticyclone used in the simulations (cross-section velocity, v, is in color). (b) Vertical structure of the square of the buoyancy frequency, N^2, for the simulation with (blue) and without (red) a jump in stratification. Snapshots of the vertical shear at 72 and 96 hours into the simulation for the runs with a jump in stratification (c)-(d), without a jump in stratification (e)-(f), and the difference between the two runs (g)-(h). Magenta arrows indicate the direction of energy propagation of NIW beams in shear and shear difference. An animation of panels (c)-(h) can be found in the supplementary material.

Acknowledgments. We are grateful to the captain and crew of the R/V *Neil Armstrong* who made the collection of these observations possible. This work was supported by ONR Grants N00014-18-1-2798 (L.N.T.), N00014-18-1-2780 (L.R. and C.M.L.), N00014-18-1-2788 (J.N.M.), and N00014-18-1-2398 and N00014-18-1-2801 (E. K.) under the NISKINe Directed Research Initiative. The comments from Amanda Vanegas Ledesma helped to improve the article.

APPENDIX -Box-

Theory for the reflection off a jump in stratification

The full solution to the wave equation involves three waves, an incident wave that propagates downwards from the surface, a transmitted wave which propagates downwards beneath the jump in stratification, and a reflected wave that propagates upwards from the jump in stratification. In the simplest case of a stationary barotropic background flow, the wave equation is separable and the vertical structure of an arbitrary wave quantity $\eta(z)$ satisfies

$$\frac{\mathrm{d}^2\eta}{\mathrm{d}z^2} + \Lambda^2 N^2(z)\eta = 0 \qquad \text{(-Box-1)}$$

where Λ is a constant of separation depending on the frequency and horizontal structure of the wave (Pollard 1970).

Away from the jump, where the WKBJ approximation is valid, we can infer the vertical wavelengths from the stratification as the vertical wavenumber, m, is proportional to the buoyancy frequency, N, (e.g. Gill 1984). As a wave propagates into more stratified water, its wavelength decreases. We can then infer the amplitude of the waves by considering the wave energy flux. The vertical wave energy flux is the product of the energy density, which is proportional to the velocity squared, and the vertical group velocity. For NIWs the vertical group velocity, $c_g \approx -N^2k^2/fm^3$, scales as $N^2/m^3 \sim 1/N$, where k is the horizontal wavenumber. The decrease in wavelength and group velocity (which determines the wavepacket velocity) with N are both captured by the ray-tracing calculations (Fig 6a-c).

Across the jump, the wave energy flux of the incident wave is conserved but split between reflected and transmitted waves. The distribution of this split depends on the vertical wavelength of the wave and details of the jump in stratification. We can consider two limiting behaviors. Firstly, the limit in which the stratification varies over a length scale much larger than the wavelength of the waves. This is the WKBJ limit and all of the wave energy flux goes to the transmitted wave with no reflection. The other limiting case is a discontinuous jump in stratification from $N = N_+$ above to $N = N_-$ below. Matching solutions to (-Box-1) for constant N above and below the jump, we find a fraction

$$R = \left(\frac{N_- - N_+}{N_- + N_+}\right)^2 \qquad \text{(-Box-2)}$$

of the wave energy flux is reflected. If the buoyancy frequency jumps by a factor of 6, as in the observations, just over half ($R = 25/49$) of the wave energy flux is reflected.

However, it is important to emphasize the distinction between the wave energy flux and the energy density. In this case, the wave energy flux of the transmitted wave is approximately half of the wave energy flux of the incident wave but, due to the change in stratification, the vertical wavelength and group velocity have been reduced by a factor of 6. As a result, the energy density and, to an even greater extent, the shear variance increase below the jump.

In reality, the change in stratification is not discontinuous but occurs over a finite vertical extent. This introduces a dependence on the wavenumber, m, of the incident wave that we explored by solving (-Box-1) for profiles of N with a $\tanh(z/h)$ transition (Fig. 6d). The fraction of wave energy flux reflected decreases monotonically as a function of mh. In the long wave limit, $mh \ll 1$, the change in stratification behaves as a discontinuous jump and the WKBJ limit (R = 0) is recovered for $mh > 1$. A similar analysis, in the absence of rotation, also found the WKBJ limit to be recovered when $mh \sim 1$ (Nault and Sutherland 2007). However, given the very sharp change in stratification and the much longer vertical wavelengths of the NIWs, the observations presented here are firmly in the long wave limit and we should expect around half the wave energy flux to be reflected.

References

Anis, A., and J. N. Moum, 1994: Prescriptions for heat flux and entrainment rates in the upper ocean during convection. *Journal of Physical Oceanography*, **24 (10)**, 2142 – 2155, https://doi.org/10.1175/1520-0485(1994)024⟨2142:PFHFAE⟩2.0.CO;2, URL https://journals.ametsoc.org/view/journals/phoc/24/10/1520-0485_1994_024_2142_pfhfae_2_0_co_2.xml.

Asselin, O., and W. R. Young, 2020: Penetration of wind-generated near-inertial waves into a turbulent ocean. *J. Phys. Oceanogr.*, **50 (6)**, 1699–1716.

Becherer, J., J. Moum, J. Colosi, J. Lerczak, and J. McSweeney, 2020: Turbulence asymmetries in bottom boundary layer velocity pulses associated with onshore-propagating nonlinear internal waves. *J. Phys. Oceanogr.*, **50**, 2373–2391.

Byun, S. S., J. J. Park, K. I., and R. W. Schmitt, 2010: Observation of near-inertial wave reflections within the thermostad layer of an anticyclonic mesoscale eddy. *Geophys. Res. Lett.*, **37**, L01 606.

Cuypers, Y., P. Bouruet-Aubertot, C. Marec, and J. L. Fuda, 2012: Characterization of turbulence from a fine-scale parameterization and microstructure measurements in the Mediterranean Sea during the boum experiment. *Biogeosciences*, **9**, 3131–3149.

D'Asaro, E. A., and H. Perkins, 1984: A near-inertial internal wave spectrum for the Sargasso Sea in late summer. *J. Phys. Oceanogr.*, **14**, 489–505.

Essink, S., E. Kunze, R. Lien, R. Inoue, and S. Ito, 2022: Near-inertial wave interactions and turbulence production in a Kuroshio anticyclonic eddy. *J. Phys. Oceanogr.*, **52**, 2687–2704.

Fer, I., A. Bosse, B. Ferron, and P. Bouruet-Aubertot, 2018: The dissipation of kinetic energy in the Lofoten Basin Eddy. *J. Phys. Oceanogr.*, **48**, 1299–1316.

Ferrari, R., and C. Wunsch, 2010: The distribution of eddy kinetic and potential energies in the global ocean. *Tellus A*, **62**, 92–108.

Gill, A. E., 1984: On the behavior of internal waves in the wakes of storms. *J. Phys. Oceanogr.*, **14**, 1129–1151.

Girton, J. B., C. Whalen, and R. Lien, 2024: Coherent float arrays for near-inertial wave studies. *Oceanography*, submitted.

Kawaguchi, Y., S. Nishino, J. Inoue, K. Maeno, H. Takeda, and K. Oshima, 2016: Enhanced diapycnal mixing due to near-inertial internal waves propagating through an anticyclonic eddy in the ice-free Chukchi Plateau. *J. Phys. Oceanogr.*, **46**, 2457–2481.

Kunze, E., 1985: Near-inertial wave propagation in geostrophic shear. *J. Phys. Oceanogr.*, **15**, 544–565.

Kunze, E., 1986: The mean and near-inertial velocity fields in a Warm-Core Ring. *J. Phys. Oceanogr.*, **16**, 1444–1461.

Kunze, E., R. Lien, C. B. Whalen, J. B. Girton, B. Ma, and M. C. Buijsman, 2023: Seasonal variability of near-inertial/semidiurnal fluctuations and turbulence in the Sub-Arctic North Atlantic. *J. Phys. Oceanogr.*, **53**, 2717–2735.

Kunze, E., and T. Sanford, 1984: Observations of near-inertial waves in a front. *J. Phys. Oceanogr.*, **14**, 566–581.

Kunze, E., R. W. Schmidt, and J. M. Toole, 1995: The energy balance in a warm-core ring's near-inertial critical layer. *J. Phys. Oceanogr.*, **25**, 942–957.

Leaman, K. D., and T. B. Sanford, 1975: Vertical energy propagation of internal waves: A vector spectral analysis of velocity profiles. *J. Geophys. Res.*, **80**, 1975–1978.

Lee, D. K., and P. P. Niiler, 1998: The inertial chimney: The near-inertial energy drainage from the ocean surface to the deep layer. *J. Geophys. Res.*, **103**, 7579–7591.

Lighthill, J., 1978: *Waves in Fluids*. Cambridge University Press, Cambridge.

Lombardo, C. P., and M. C. Gregg, 1989: Similarity scaling of viscous and thermal dissipation in a convecting surface boundary layer. *J. Geophys. Res.*, **94**, 6273–6284.

Lueck, R., and T. Osborn, 1986: The dissipation of kinetic energy in a warm-core ring. *J. Geophys. Res.*, **91(C1)**, 803–818.

Mooers, C. N. K., 1975: Several effects of a baroclinic current on the cross-stream propagation of inertial-internal waves. *Geophys. Fluid Dyn.*, **6**, 245–275.

Moum, J. N., and J. D. Nash, 2009: Mixing measurements on an equatorial ocean mooring. *J. Atmos. Oceanic Technol.*, **26**, 317–336, https://doi.org/10.1175/2008JTECHO617.1.

Moum, J. N., W. D. Smyth, K. G. Hughes, D. Cherian, S. J. Warner, B. Bourles, P. Brandt, and M. Dengler, 2023: Wind dependencies of deep cycle turbulence in the equatorial cold tongues. *J. Phys. Oceanogr.*, **53**, 1975–1995, https://doi.org/10.1175/JPO-D-22-0203.1.

Nault, J. T., and B. R. Sutherland, 2007: Internal wave transmission in nonuniform flows. *Physics of Fluids*, **19 (1)**, 016 601, https://doi.org/10.1063/1.2424791.

Olbers, D. J., 1981: The propagation of internal waves in a geostrophic current. *J. Phys. Oceanogr.*, **11**, 1224–1233.

Pollard, R. T., 1970: On the generation by winds of inertial waves in the ocean. *Deep Sea Research and Oceanographic Abstracts*, **17 (4)**, 795–812, https://doi.org/10.1016/0011-7471(70)90042-2.

Pollard, R. T., and R. C. Millard, 1970: Comparison between observed and simulated wind-generated inertial oscillations. *Deep-Sea Res.*, **17**, 153–175.

Shchepetkin, A. F., and J. C. McWilliams, 2005: The regional oceanic modeling system (roms): a split-explicit, free-surface, topography-following-coordinate oceanic model. *Ocean Modelling*, **9 (4)**, 347–404.

Thomas, L. N., L. Rainville, O. Asselin, W. R. Young, J. B. Girton, C. B. Whalen, L. R. Centurioni, and V. Hormann, 2020: Direct observations of near-inertial wave ζ-refraction in a dipole vortex. *Geophys. Res. Lett.*, **47**, e2020GL090 375.

Thomas, L. N., E. D. Skyllingstad, L. Rainville, V. Hormann, L. Centurioni, J. N. Moum, O. Asselin, and C. M. Lee, 2023: Damping of inertial motions through the radiation of near-inertial waves in a dipole vortex in the Iceland Basin. *J. Phys. Oceanogr.*, in press.

Vic, C., B. Ferron, V. Thierry, H. Mercier, and P. Lherminier, 2021: Tidal and near-inertial internal waves over the Reykjanes Ridge. *J. Phys. Oceanogr.*, **51**, 419–437.

Waterhouse, A. F., and Coauthors, 2022: Global observations of rotary-with-depth shear spectra. *J. Phys. Oceanogr.*, **52**, 3241–3258.

Whalen, C. B., J. A. MacKinnon, and L. D. Talley, 2018: Large-scale impacts of the mesoscale environment on mixing from wind-driven internal waves. *Nature Geo.*, **11**, 842–847.

Whitt, D. B., and L. N. Thomas, 2013: Near-inertial waves in strongly baroclinic currents. *J. Phys. Oceanogr.*, **43**, 706–725.

Zhang, Y., and J. N. Moum, 2010: Inertial-convective subrange estimates of thermal variance dissipation rate from moored temperature measurements. *J. Atmos. Oceanic Technol.*, **27**, 1950–1959, https://doi.org/10.1175/2010JTECHO746.1.